Nature of the Insulating Ground State of the 5*d* Postperovskite $CaIrO_3$

Sun-Woo Kim,[1] Chen Liu,[2] Hyun-Jung Kim,[1,3] Jun-Ho Lee,[1,4] Yongxin Yao,[2,†] Kai-Ming Ho,[2,3] and Jun-Hyung Cho[1,3,*]
[1]*Department of Physics and Research Institute for Natural Sciences, Hanyang University, 17 Haengdang-Dong, Seongdong-Ku, Seoul 133-791, Korea*
[2]*Ames Laboratory and Department of Physics and Astronomy, Iowa State University, Ames, Iowa 50011, USA*
[3]*International Center for Quantum Design of Functional Materials (ICQD), HFNL, University of Science and Technology of China, Hefei, Anhui 230026, China*
[4]*Korea Institute for Advanced Study, 85 Hoegiro, Dongdaemun-gu, Seoul 130-722, Korea*
(Received 29 December 2014; published 26 August 2015)

The insulating ground state of the 5*d* transition metal oxide $CaIrO_3$ has been classified as a Mott-type insulator. Based on a systematic density functional theory (DFT) study with local, semilocal, and hybrid exchange-correlation functionals, we reveal that the Ir t_{2g} states exhibit large splittings and one-dimensional electronic states along the *c* axis due to a tetragonal crystal field. Our hybrid DFT calculation adequately describes the antiferromagnetic (AFM) order along the *c* direction via a superexchange interaction between Ir^{4+} spins. Furthermore, the spin-orbit coupling (SOC) hybridizes the t_{2g} states to open an insulating gap. These results indicate that $CaIrO_3$ can be represented as a spin-orbit Slater insulator, driven by the interplay between a long-range AFM order and the SOC. Such a Slater mechanism for the gap formation is also demonstrated by the DFT + dynamical mean field theory calculation, where the metal-insulator transition and the paramagnetic to AFM phase transition are concomitant with each other.

DOI: 10.1103/PhysRevLett.115.096401 PACS numbers: 71.20.Be, 71.15.Mb, 71.70.Ej, 75.10.Lp

One of the most important phenomena in condensed matter physics is the Mott transition driven by electron-electron correlations [1,2]. In 3*d* transition-metal oxides (TMOs), the localized 3*d* orbitals are responsible for the strong on-site Coulomb repulsion (U), leading to a Mott-Hubbard insulator where U splits a half-filled band into lower and upper Hubbard bands. Surprisingly, despite weaker U in 5*d* TMOs due to the very delocalized 5*d* orbitals, a series of Ir oxides such as Sr_2IrO_4 [3–7], Na_2IrO_3 [8–10], and $CaIrO_3$ [11–15] including Ir^{4+} ions with five valence electrons exhibit an insulating ground state. For this unusual insulating behavior of the 5*d* iridates, it was proposed that spin-orbit coupling (SOC) splits the Ir t_{2g} states into completely filled $j_{\text{eff}} = 3/2$ bands and a narrow half-filled $j_{\text{eff}} = 1/2$ band at the Fermi level (E_F), and the latter band is further split into two Hubbard subbands by moderate Coulomb repulsion [3–5]. Such a $j_{\text{eff}} = 1/2$ Mott-Hubbard scenario has, however, been challenged by an alternative scenario of Slater mechanism [16] based on the single-particle band picture, where the opening of insulating gap in 5*d* TMOs is driven by a long-range magnetic ordering [6,7,17,18].

Here we focus on the postperovskite $CaIrO_3$ with a highly anisotropic geometry where IrO_6 octahedra share corners along the *c* axis and have common edges along the *a* axis (see Fig. 1). Recently, the nature of the ground state in $CaIrO_3$ has been an object of hot debate [11–15]. On the basis of resonant x-ray magnetic scattering (RMXS) experiment, Ohgushi *et al.* [12] claimed the robustness of the $j_{\text{eff}} = 1/2$ ground state against structural distortions. However, a resonant inelastic x-ray scattering (RIXS) experiment of Sala *et al.* [13] concluded that $CaIrO_3$ is not a $j_{\text{eff}} = 1/2$ iridate by showing that the $j_{\text{eff}} = 1/2$ state is severely altered by a large tetragonal crystal field splitting, therefore proposing the existence of the Mott insulator beyond the $j_{\text{eff}} = 1/2$ ground state. On the theoretical side, using density-functional theory (DFT) calculations within the local density approximation (LDA) including SOC, Subedi [14] interpreted the t_{2g} states in terms of the $j_{\text{eff}} = 1/2$ and $j_{\text{eff}} = 3/2$ states, and further showed that the introduction of U splits the $j_{\text{eff}} = 1/2$ bands into fully

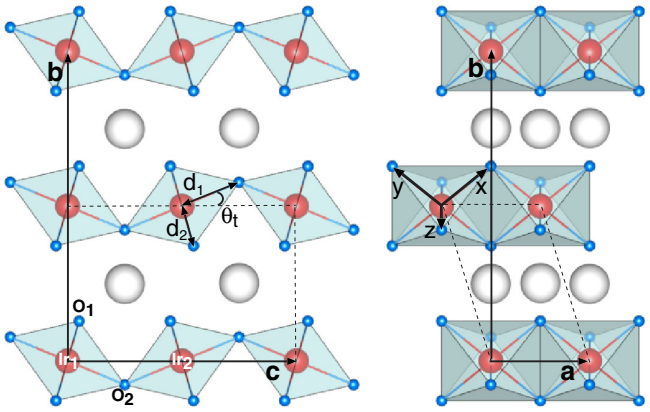

FIG. 1 (color online). Crystal structure of $CaIrO_3$ projected on the *bc* plane (left side) and the *ab* plane (right side). *a*, *b*, and *c* denote unit vectors of the conventional unit cell. The primitive unit cell is indicated by the dashed lines. The large, medium, and small circles represent Ca, Ir, and O atoms, respectively. The bond lengths (d_1 and d_2) and the tilt angle (θ_t) are indicated for Table IS [19]. The reference frame *xyz* is drawn in an IrO_6 octahedron.

occupied lower and unoccupied upper Hubbard bands, thereby supporting the Mott-Hubbard scenario. Contrasting with the $j_{\rm eff} = 1/2$ ground state generated by equally hybridizing the three d_{xy}, d_{yz}, and d_{zx} orbitals [12], *ab initio* wave-function quantum chemical calculation [15] predicted the highly uneven admixture of xy, yz, and zx characters for the relativistic t_{2g} states. Therefore, previous experimental and theoretical studies of $CaIrO_3$ have not reached a consensus on the presence of the $j_{\rm eff} = 1/2$ ground state, but concluded in the same way that $CaIrO_3$ belongs to a Mott-Hubbard insulator. Despite such a contradiction for the nature of the ground state, it is well established [12–15] that the insulating ground state of $CaIrO_3$ exhibits the stripe-type magnetic order with a strong antiferromagnetic (AFM) coupling along the c axis and a weak ferromagnetic one along the a axis (hereafter designated as the AFM structure).

In this Letter, we investigate the nature of the ground state of $CaIrO_3$ by using comprehensive DFT calculations with local, semilocal, and hybrid exchange-correlation functionals as well as by including dynamical mean field theory (DMFT). We find that the t_{2g} states are significantly split by a compression of IrO_6 octahedra along the c axis and particularly two t_{2g} states (designated as t_{2g}^{S1} and t_{2g}^{S2}) have dominant d_{yz} and d_{zx} characters with large band dispersions, indicating one-dimensional (1D) electronic states along the c axis. Our hybrid DFT calculation adequately describes the delocalized t_{2g}^{S1} and t_{2g}^{S2} states to stabilize the AFM order along the c axis via superexchange interaction between Ir^{4+} spins. Moreover, the SOC is found to hybridize the t_{2g}^{S1} and t_{2g}^{S2} states with other t_{2g} states to open an insulating gap. It is thus elucidated that the gap formation in $CaIrO_3$ is driven by the interplay between a long-range AFM order and the SOC, representing a spin-orbit Slater insulator. This Slater mechanism for the gap formation in $CaIrO_3$ is further supported by the DFT + DMFT calculation.

We first study the ground state of $CaIrO_3$ using the LDA, GGA, and hybrid DFT calculations [27] without SOC. Interestingly, the different ground states are predicted depending on the employed exchange-correlation functionals: i.e., the CA functional predicts the nonmagnetic (NM) ground state, while the PBE and HSE functionals favor the AFM structure over the NM structure by $\Delta E_{\rm NM\text{-}AFM} = 21.1$ and 85.8 meV per primitive unit cell, respectively. The calculated structural parameters of Ir-O bond lengths (d_1 and d_2 in Fig. 1) and tilt angle (θ_t in Fig. 1) change little depending on the employed exchange-correlation functionals. Our values of $d_1/d_2 \approx 0.96$ and $\theta_t \approx 23°$ indicate that the IrO_6 octahedra are compressed along the c axis with a large tilt, in good agreement with an XRD analysis [28] and a previous LDA calculation [14] (see Table IS of the Supplemental Material [19]). Figure 2(a) shows the LDA band structure of the NM structure together with d-orbitals projected bands and the charge characters of the t_{2g} states. There are six t_{2g} bands originating from two different Ir atoms within the primitive unit cell, which are grouped into two doublets (t_{2g}^{D1} and t_{2g}^{D2}) and two singlets (t_{2g}^{S1} and t_{2g}^{S2}). We find the presence of partially occupied t_{2g} states crossing E_F, indicating a metallic feature. It is seen in Fig. 2(a) that (i) the t_{2g}^{D1} and t_{2g}^{D2} doublets are significantly separated by ~1.5 eV at the Γ point and (ii) the low(high)-lying t_{2g}^{D2} (t_{2g}^{D1}) states involve dominantly d_{xy} (d_{yz} and d_{zx}) component(s). These different orbital characters of t_{2g}^{D1} and t_{2g}^{D2} can be attributed to a tetragonal crystal field due to the compressed IrO_6 octahedra along the c axis. In addition, the t_{2g}^{S1} and t_{2g}^{S2} states also have dominant d_{yz} and d_{zx} characters with a large bandwidth of ~2.5 eV, indicating 1D electronic states along the c axis. As shown in the inset in Fig. 2(a), the charge character of t_{2g}^{S1} (or t_{2g}^{S2}) shows a strong hybridization with O $2p$ orbitals along the c axis, reflecting its 1D band feature. This 1D feature of the t_{2g}^{S1} and t_{2g}^{S2} states plays an important role in determining the electronic and magnetic properties of $CaIrO_3$, as discussed below.

Figure 2(b) and 2(c) show the PBE and HSE band structures of the AFM structure, respectively. Here, the overall band dispersion of the AFM structure is similar to that [Fig. 2(a)] of the NM structure. However, there are two conspicuous changes in the AFM band structure: i.e., one is a gap opening E_g^{S1-S2} of the t_{2g}^{S1} and t_{2g}^{S2} singlets at the T point and the other is some separation of the two bands in the t_{2g}^{D1}

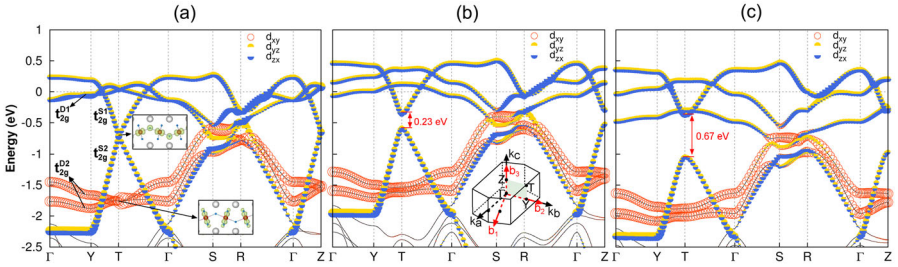

FIG. 2 (color online). Band structures of (a) the NM structure obtained using LDA, (b) the AFM structure obtained using PBE, and (c) the AFM structure obtained using HSE. The band dispersions are plotted along the path $\Gamma(0,0,0) \rightarrow Y(0,0.5,0) \rightarrow T(0,0.5,0.5) \rightarrow \Gamma(0,0,0) \rightarrow S(0.25,0.25,0) \rightarrow R(0.25,0.25,0.5) \rightarrow \Gamma(0,0,0) \rightarrow Z(0,0,0.5)$ in the Brillouin zone of the unit cell [see the inset in (b)]. The energy zero represents the Fermi level. The bands projected onto d_{xy}, d_{yz}, and d_{zx} orbitals are also displayed. Here, the radii of circle and semicircles are proportional to the weights of corresponding orbitals. In (a), the charge characters of t_{2g}^{S1} and t_{2g}^{D2} states at the T point are shown with an isosurface of 0.02 $e/\text{Å}^3$.

TABLE I. Spin magnetic moments (in units of μ_B) of Ir, O_1, and O_2 atoms obtained using the PBE, HSE, PBE + SOC, and HSE + SOC calculations. The calculated orbital magnetic moments using PBE + SOC and HSE + SOC are given in parentheses. O_1 is placed in the ab plane while O_2 represents the corner-sharing O atom along the c axis (see Fig. 1).

	Ir	O_1	O_2
PBE	0.31	0.05	0.00
HSE	0.48	0.07	0.00
PBE + SOC	0.16(0.08)	0.02(0.00)	0.00(0.00)
HSE + SOC	0.45(0.34)	0.05(0.01)	0.01(0.01)

doublet. We obtain $E_g^{S1-S2} = 0.23$ eV [Fig. 2(b)] and 0.67 eV [Fig. 2(c)] from PBE and HSE, respectively. To understand the microscopic mechanism for these changes in the AFM band structure, we plot the spin-polarized d-orbitals projected bands (see Fig. 1S of the Supplemental Material [19]). We find that the t_{2g}^{S1} and t_{2g}^{S2} states (or the two states in t_{2g}^{D1}) with the same spin direction, localized at two different Ir sites, hybridize with each other, yielding an energy gain from the exchange kinetic energy and the formation of E_g^{S1-S2} [29]. This so-called superexchange interaction [30,31] between Ir^{4+} spins results in the stabilization of the AFM order along the c axis. Our finding that the t_{2g}^{S1}, t_{2g}^{S2}, and t_{2g}^{D1} states with d_{yz} and d_{zx} characters are associated with the AFM order does not support the interpretation of the previous RMXS experiment [12] that the $j_{\text{eff}} = 1/2$ state stabilizes the AFM order. In Table I, we list the calculated magnetic moments of Ir and O atoms in the AFM structure. Our HSE calculation gives a spin magnetic moment $m_S = 0.48$ (0.07) μ_B for Ir (O_1) atoms, larger than $m_S = 0.31$ (0.05) μ_B computed using PBE. We note that the LDA and GGA tend to stabilize artificially delocalized electronic states due to their inherent self-interaction error because delocalization reduces the spurious self-repulsion of electrons [32,33]. This aspect of LDA and GGA may account for why our LDA calculation predicts a metallic NM ground state and our PBE values of $\Delta E_{\text{NM-AFM}}$ and m_S are relatively smaller than the corresponding HSE ones (see Table I).

Next, we examine the effect of SOC on the geometry and band structure of the AFM structure using PBE + SOC and HSE + SOC [27]. As shown in Table IS of the Supplemental Material, the inclusion of SOC changes little d_1/d_2 and θ_t by less that 0.01 and 1°, respectively. Figures 3(a) and 3(b) show the PBE + SOC and HSE + SOC band structures of the AFM structure, respectively. Compared to the PBE [Fig. 2(b)] and HSE [Fig. 2(c)] results, d-orbitals projected bands clearly show that the inclusion of SOC does not change the d_{xy}, d_{yz}, and d_{zx} characters of the t_{2g}^{D1}, t_{2g}^{D2}, t_{2g}^{S1} and t_{2g}^{S2} states but gives rise to their strong hybridizations leading to well-separated t_{2g} bands with hybridization gaps. This result does not support the $j_{\text{eff}} = 1/2$ ground-state picture proposed by the RMXS experiment [12], where SOC can dramatically affect the t_{2g} states to produce the $j_{\text{eff}} = 1/2$ state by equally mixing up the d_{xy}, d_{yz}, and d_{zx} orbitals. We note that for the t_{2g} state near E_F, the partial densities of states (PDOS) of the d_{xy}, d_{yz}, and d_{zx} orbitals obtained using HSE give a ratio of 0%:50%:50%, but change into 8%:46%:46% for the HSE + SOC calculation [see Fig. 2S of the Supplemental Material]. The latter PDOS ratio of d_{xy}, d_{yz}, and d_{zx} is very consistent with the interpretation of RIXS experiment [13] that the t_{2g} state near E_F was estimated as $\mp 0.32|xy, \mp > + 0.67$ ($|yz, \pm > \mp i|zx, \pm >$). As a consequence of the SOC-induced hybridization, PBE + SOC still does not open an insulating gap [Fig. 3(a)], but HSE + SOC opens $E_g = 0.32$ eV [Fig. 3(b)], close to the experimental data of ~0.34 eV [11]. Especially, the DOS [see Fig. 3(b)] obtained using HSE + SOC explains well the two d-d interband transitions observed in the RIXS experiment [34]. It is noteworthy that the gap opening in HSE + SOC can be realized by the strong interplay between a long-range AFM order and the SOC; i.e., the enhanced separation of the t_{2g}^{S1} and t_{2g}^{D1} bands in the AFM structure [see Fig. 2(c)] and the SOC-induced hybridization are combined to yield the opening of an insulating gap. Thus, we can say that the single-particle band theory within the HSE + SOC scheme predicts well the magnetic-insulating ground state of $CaIrO_3$, being represented as a spin-orbit Slater insulator.

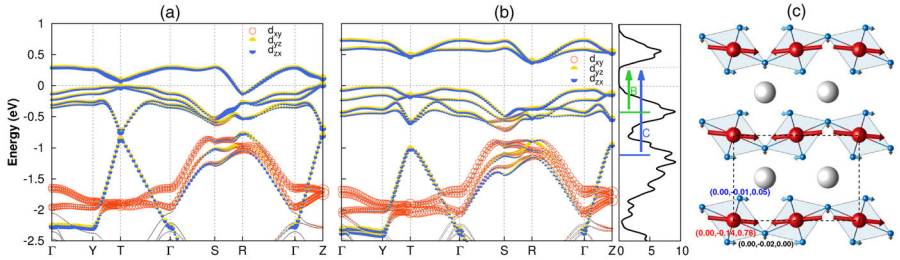

FIG. 3 (color online). Band structure of the AFM structure, obtained using the (a) PBE + SOC and (b) HSE + SOC calculations. The DOS obtained using HSE+SOC is also given in (b). The theoretical estimation of the B and C features observed from RIXS experiment [13] is drawn in DOS. In (c), the sum of the spin and orbital magnetic moments obtained using the HSE + SOC calculation is drawn with three components (m_a, m_b, m_c) along the a, b, and c axes. Here, m_i is calculated by integrating the corresponding component of the magnetic moment inside the PAW sphere with a radius of 1.4 (0.8) Å for Ir (O).

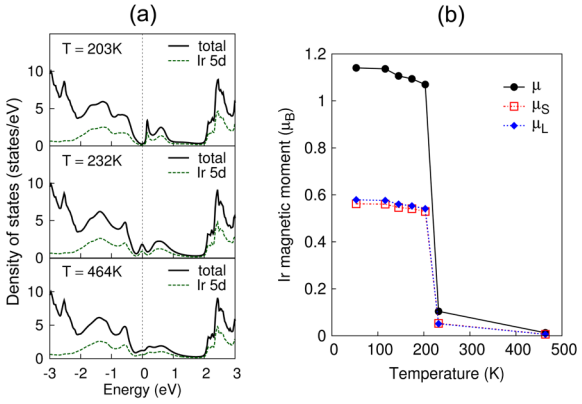

FIG. 4 (color online). (a) Density of states with respect to temperature, obtained using the DFT + DMFT calculation. The calculated magnetic moment (μ) of Ir atom as a function of temperature is plotted in (b), together with spin (μ_S) and orbital (μ_L) components.

Figure 3(c) shows the sum of the spin and orbital magnetic moments of Ir and O atoms, obtained using HSE + SOC. The total magnetic moment for Ir, O_1, and O_2 atoms is (0.00, −0.14, ±0.78), (0.00, −0.01, ±0.05), and (0.00, −0.02, 0.00) in units of μ_B, respectively, showing an antiparallel alignment of magnetic moments along the c axis. Here, the Ir magnetic moments are canted along the b axis with ∼11°, comparable with those (2–4°) reported from RMXS [12] and RIXS [13] experiments.

Finally, in order to confirm the Slater mechanism for the gap formation in $CaIrO_3$, we perform the DFT + DMFT calculation [19,35] for the AFM and paramagnetic phases. Figure 4(a) shows the DFT + DMFT results for the one-particle spectra. It is seen that the AFM insulating phase is transformed into a paramagnetic metallic phase [36] around 230 K. Below this metal-insulator transition (MIT) temperature, the magnetic moment of the Ir atom sharply increases [see Fig. 4(b)], indicating that the MIT and the paramagnetic to AFM phase transition are concomitant with each other. The calculated spectral function for the AFM ground state is displayed in Fig. 3S of the Supplemental Material [19], together with the superimposition of the HSE + SOC band structure. Both results are in good agreement with each other. Therefore, both the comprehensive DFT calculations and the DFT + DMFT calculation reach a consistent conclusion that the gap opening is induced by the AFM order, representing a Slater-type insulator.

In conclusion, our comprehensive DFT calculations with local, semilocal, and hybrid exchange-correlation functionals clarified the effects of tetragonal crystal field, AFM order, and SOC on the t_{2g} states of $CaIrO_3$. We found the large tetragonal crystal field splitting of the t_{2g} states, resulting in the formations of t_{2g}^{D1} doublet (with d_{yz} and d_{zx} characters), t_{2g}^{D2} doublet (with d_{xy} character), and t_{2g}^{S1} and t_{2g}^{S2} singlets (with d_{yz} and d_{zx} characters). We also found that the insulating-gap opening is formed by the interplay between a long-range AFM order and the SOC, representing a spin-orbit Slater insulator. This single-particle-based Slater picture is further supported by the DFT+DMFT calculation. Our findings are anticipated to stimulate further experimental and theoretical studies for other iridates such as Sr_2IrO_4 [3–5] and Na_2IrO_3 [8–10] which have been proposed to be a $j_{\text{eff}} = 1/2$ Mott-Hubbard insulator.

This work was supported in part by National Research Foundation of Korea (NRF) grant funded by the Korea Government (2015R1A2A2A01003248), by Program of Introducing Talents of Discipline to Universities of Ministry of Education (MOE) & the State Administration of Foreign Experts Affairs of the People's Republic of China (SAFEA), and by NSFC (Grant No. 61434002). The calculations were performed by KISTI supercomputing center through the strategic support program (KSC-2014-C3-011) for the supercomputing application research. Research at Ames Laboratory was supported by the U.S. DOE, Office of Basic Energy Sciences, Division of Materials Sciences and Engineering. Ames Laboratory is operated for the U.S. Department of Energy by Iowa State University under Contract No. DE-AC02-07CH11358.

*Corresponding author.
chojh@hanyang.ac.kr
†Corresponding author.
ykent@iastate.edu

[1] N. F. Mott, *Metal-Insulator Transitions* (Taylor & Francis, London/Philadelphia, 1990).
[2] M. Imada, A. Fujimori, and Y. Tokura, Rev. Mod. Phys. **70**, 1039 (1998).
[3] B. J. Kim, H. Jin, S. J. Moon, J.-Y. Kim, B.-G. Park, C. S. Leem, J. Yu, T. W. Noh, C. Kim, S.-J. Oh, J.-H. Park, V. Durairaj, G. Cao, and E. Rotenberg, Phys. Rev. Lett. **101**, 076402 (2008).
[4] B. J. Kim, H. Ohsumi, T. Komesu, S. Sakai, T. Morita, H. Takagi, and T. Arima, Science **323**, 1329 (2009).
[5] S. J. Moon, H. Jin, W. S. Choi, J. S. Lee, S. S. A. Seo, J. Yu, G. Cao, T. W. Noh, and Y. S. Lee, Phys. Rev. B **80**, 195110 (2009).
[6] R. Arita, J. Kuneš, A. V. Kozhevnikov, A. G. Eguiluz, and M. Imada, Phys. Rev. Lett. **108**, 086403 (2012).
[7] Q. Li, G. Cao, S. Okamoto, J. Yi, W. Lin, B. C. Sales, J. Yan, R. Arita, J. Kuneš, A. V. Kozhevnikov, A. G. Eguiluz, M. Imada, Z. Gai, M. Pan, and D. G. Mandrus, Sci. Rep. **3**, 3073 (2013).
[8] A. Shitade, H. Katsura, J. Kuneš, X.-L Qi, S.-C. Zhang, and N. Nagaosa, Phys. Rev. Lett. **102**, 256403 (2009).
[9] R. Comin, G. Levy, B. Ludbrook, Z.-H. Zhu, C. N. Veenstra, J. A. Rosen, Y. Singh, P. Gegenwart, D. Stricker, J. N. Hancock, D. van der Marel, I. S. Elfimov, and A. Damascelli, Phys. Rev. Lett. **109**, 266406 (2012).
[10] H. Gretarsson, J. P. Clancy, X. Liu, J. P. Hill, E. Bozin, Y. Singh, S. Manni, P. Gegenwart, J. Kim, A. H. Said, D. Casa, T. Gog, M. H. Upton, H.-S. Kim, J. Yu, V. M. Katukuri, L. Hozoi, J. van den Brink, and Y.-J. Kim, Phys. Rev. Lett. **110**, 076402 (2013).

[11] K. Ohgushi, H. Gotou, T. Yagi, Y. Kiuchi, F. Sakai, and Y. Ueda, Phys. Rev. B **74**, 241104 (2006).
[12] K. Ohgushi, J.-I. Yamaura, H. Ohsumi, K. Sugimoto, S. Takeshita, A. Tokuda, H. Takagi, M. Takata, and T.-H. Arima, Phys. Rev. Lett. **110**, 217212 (2013).
[13] M. M. Sala, K. Ohgushi, A. Al-Zein, Y. Hirata, G. Monaco, and M. Krisch, Phys. Rev. Lett. **112**, 176402 (2014).
[14] A. Subedi, Phys. Rev. B **85**, 020408 (2012).
[15] N. A. Bogdanov, V. M. Katukuri, H. Stoll, J. van den Brink, and L. Hozoi, Phys. Rev. B **85**, 235147 (2012).
[16] J. C. Slater, Phys. Rev. **82**, 538 (1951).
[17] S. Calder, V. O. Garlea, D. F. McMorrow, M. D. Lumsden, M. B. Stone, J. C. Lang, J.-W. Kim, J. A. Schlueter, Y. G. Shi, K. Yamaura, Y. S. Sun, Y. Tsujimoto, and A. D. Christianson, Phys. Rev. Lett. **108**, 257209 (2012).
[18] H.-J. Kim, J.-H. Lee, and J.-H. Cho, Sci. Rep. **4**, 5253 (2014).
[19] See Supplemental Material at http://link.aps.org/supplemental/10.1103/PhysRevLett.115.096401, which includes Refs. [20–26], for the structural parameters of the optimized structures, the spin-polarized d-orbitals projected band structures, the PDOS of the d_{xy}, d_{yz}, and d_{zx} orbitals, the computational details of the DFT + DMFT calculation, and the spectral function of the AFM state obtained using the DFT + DMFT calculation.
[20] K. Haule, C.-H. Yee, and K. Kim, Phys. Rev. B **81**, 195107 (2010).
[21] J. P. Perdew, K. Burke, and M. Ernzerhof, Phys. Rev. Lett. **77**, 3865 (1996); **78**, 1396(E) (1997).
[22] P. Blaha, K. Schwarz, G. K. H. Madsen, D. Kvasnicka, and J. Luitz, *WIEN2k, An Augmented Plane Wave + Local Orbitals Program for Calculating Crystal Properties* (Karlheinz Schwarz, Techn. Universit at Wien, Austria, 2001), ISBN 3-9501031-1-2.
[23] P. Werner, A. Comanac, L. de Medici, M. Troyer, and A. J. Millis, Phys. Rev. Lett. **97**, 076405 (2006).
[24] K. Haule, Phys. Rev. B **75**, 155113 (2007).
[25] A. Kutepov, K. Haule, S. Y. Savrasov, and G. Kotliar, Phys. Rev. B **82**, 045105 (2010).
[26] H. Zhang, K. Haule, and D. Vanderbilt, Phys. Rev. Lett. **111**, 246402 (2013).
[27] We have performed not only the local (LDA), semilocal (GGA), and hybrid DFT calculations using the Vienna *ab initio* simulation package (VASP) with the projector augmented wave method [Kresse and Hafner, Phys. Rev. B **48**, 13115 (1993); Kresse and Furthmüller, Comput. Mater. Sci. **6**, 15 (1996)] but also the DFT + DMFT calculation using the WIEN2K package (see Supplemental Material). For the exchange-correlation energy, we employed the LDA functional of Ceperley-Alder (CA); [Ceperley and Alder, Phys. Rev. Lett. **45**, 566 (1980)], the GGA functional of Perdew-Burke-Ernzerhof (PBE); [Perdew, Burke, and Ernzerhof, Phys. Rev. Lett. **77**, 3865 (1996); **78**, 1396(E) (1997)], and the hybrid functional of Heyd-Scuseria-Ernzerhof (HSE); [Heyd, Scuseria, and Erzerhof, J. Chem. Phys. **118**, 8207 (2003); A. V. Krukau, O. A. Vydrov, A. F. Izmaylov, and G. E. Scuseria , J. Chem. Phys. **125**, 224106 (2006)]. Since the HSE + SOC calculation with a mixing factor of $\alpha = 0.08$ (in the HSE functional) controlling the amount of exact Fock exchange energy predicts well the observed insulating gap of 0.34 eV [11], we used this optimal α value for the HSE and HSE + SOC calculations. We employed the primitive unit cell in the *Cmcm* structure (see Fig. 1), with the experimental lattice constants $a = 3.145$, $b = 9.855$, and $c = 7.293$ Å; [F. Rodi and D. Babel, Z. Anorg. Allg. Chem. **336**, 17 (1965)]. The **k**-space integration was done with the $9 \times 5 \times 5$ uniform meshes in the Brillouin zone. All atoms were allowed to relax along the calculated forces until all the residual force components were less than 0.01 eV/Å.
[28] S. Hirai, M. Welch, F. Aguado, and S. Redfern, Z. Kristallogr. **224**, 345 (2009).
[29] K. Sato, L. Bergqvist, J. Kudrnovsky, P. H. Dederichs, O. Eriksson, I. Turek, B. Sanyal, G. Bouzerar, H. Katayama-Yoshida, V. A. Dinh, T. Fukushima, H. Kizaki, and R. Zeller, Rev. Mod. Phys. **82**, 1633 (2010).
[30] J. B. Goodenough, Phys. Rev. **100**, 564 (1955).
[31] J. Kanamori, J. Phys. Chem. Solids **10**, 87 (1959).
[32] P. Mori-Sánchez, A. J. Cohen, and W. Yang, Phys. Rev. Lett. **100**, 146401 (2008).
[33] A. J. Cohen, P. Mori-Sánchez, and W. Yang, Science **321**, 792 (2008).
[34] For intra-t_{2g} excitations, the measured RIXS spectra were fitted to three Pearson functions in the energy range between 0.3 and 1.6 eV below the conduction band edge: i.e., a weak, energy-resolution limited peak (A) with an excitation energy of ~0.42 eV and two intense broad features (B and C) centered at 0.65 and 1.22 eV. In order to compare these RIXS excitations with our calculated t_{2g} bands, we plot the density of states obtained using HSE + SOC in Fig. 3(b). We find that the calculated DOS exhibits two well-separated energy regions below E_F, i.e., the region I from E_F to −0.8 eV and the region II from −0.8 to −1.3 eV. Here, since the intra-t_{2g} excitations in RIXS spectra were measured in the energy range between 0.3 and 1.6 eV below the conduction band edge, we take the energy range of the region II from $E_F - 0.8$ to $E_F - 1.3$ eV. We estimate the center of each region as $\epsilon_{\mathrm{I}} = -0.45$ eV and $\epsilon_{\mathrm{II}} = -1.13$ eV by using a relation of $\epsilon = \int \mathrm{DOS}(E) \times E\, dE / \int \mathrm{DOS}(E)\, dE$. Considering that the HSE + SOC band gap is 0.32 eV, the excitation energies of two d-d transitions are estimated to be 0.77 and 1.45 eV, well comparable with those (0.65 and 1.22 eV) for the B and C features in the RIXS experiment. We note that, although the observed A peak cannot be clearly identified from the calculated DOS, it may be associated with the flat t_{2g} bands near E_F [see Fig. 3(b)].
[35] G. Kotliar, S. Y. Savrasov, K. Haule, V. S. Oudovenko, O. Parcollet, and C. A. Marianetti, Rev. Mod. Phys. **78**, 865 (2006).
[36] In Ref. [11], the resistivity measurement of $CaIrO_3$ with employing a polycrystalline sample showed a paramagnetic insulating behavior above the Néel temperature. Note that the resistivity of polycrystalline iridium oxides was measured to be larger than that of single crystalline counterparts by 10^3 order because of their grain boundaries [see N. S. Kini, A. M. Strydom, H. S. Jeevan, C. Geibel, and S. Ramakrishnan, J. Phys. Condens. Matter **18**, 8205 (2006)]. More elaborate experimental tools such as photoemission spectroscopy, scanning tunneling spectroscopy, and optical spectroscopy will be anticipated to resolve the connection between the AFM order and the MIT in $CaIrO_3$.